# Water vapor condensation in porous media: Effects of fracture, porosity, and flow rate revealed by rapid 4D neutron imaging

Arash Nemati, Bratislav Lukić, Alessandro Tengattini, Matthieu Briffaut, Philippe Séchet

Advances in Water Resources 195 (2025) 104872

Contents lists available at ScienceDirect

Advances in Water Resources

journal homepage: www.elsevier.com/locate/advwatres

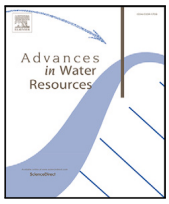

# Water vapor condensation in porous media: Effects of fracture, porosity, and flow rate revealed by rapid 4D neutron imaging

Arash Nemati [a], Bratislav Lukić [b,c,*], Alessandro Tengattini [d,e], Matthieu Briffaut [f], Philippe Séchet [a]

[a] Université Grenoble Alpes, LEGI, 38000 Grenoble, France
[b] The European Synchrotron Radiation Facility, 38043 Grenoble Cedex 9, France
[c] Henry Royce Institute, Department of Materials, The University of Manchester, UK
[d] Université Grenoble Alpes, 3SR, 38000 Grenoble, France
[e] Institute Laue-Langevin, 38042 Grenoble Cedex 9, France
[f] CNRS, Centrale Lille, UMR9013—LaMcube—Laboratoire de mécanique multiphysique et multiéchelle, Université de Lille, F-59000 Lille, France

## ARTICLE INFO

Dataset link: doi.org/10.5291/ILL-DATA.1-07-28, doi.org/10.5291/ILL-DATA.1-07-12

*Keywords:*
Neutron tomography
Fast tomography
Multi-phase flow
Condensation
Fracture
Porous media

## ABSTRACT

This study investigates water vapor condensation processes in a fractured porous medium (sandstone), focusing on the effects of fracture conductivity, matrix porosity, and imposed flow rate of the vapor. Cylindrical samples of Fontainebleau sandstone were pre-fractured using the Brazilian splitting test and subjected to a constant vapor and air mixture flow rate. Rapid *in situ* neutron tomography, captured every 30 s, visualized time-resolved water migration through the porous media. Owing to the high neutron attenuation by hydrogen, the obtained contrast allowed quantitative 3D tracking of condensed water within the material bulk. The experimental data demonstrated the reliability of neutron imaging through consistent measurements of overall water content, as verified by imposed macroscopic boundary conditions. The results showed that cracks act as preferential pathways for vapor migration, leading to the formation of initial wetting fronts and subsequent capillary absorption into the matrix from inner fracture surfaces. The presence of a crack slowed the propagation of the water front in the porous matrix, allowing more water to accumulate within it. Low porosity samples exhibited lower water contents in the matrix, resulting in faster propagation of the water front due to the limited water absorption capacity of the matrix. In this case, water accumulates in the crack in the form of water patches, especially at lower flow rates, where the vapor's exerted pressure is lower, allowing more water to remain in the porous matrix. At higher flow rates, cracks remained drier compared to the matrix due to increased injection pressure, which transferred water into the matrix more effectively. Rapid transitions of water patches were observed in the high flow rate low porosity case, highlighting dynamic water movement in the crack. The study underscores the importance of heterogeneity in the form of cracks in the absorption of condensed water and highlights the roles of capillary effects and pressure-driven flow in the transportation of water within fractured porous media. It provides novel full-field experimental datasets, which are invaluable for further numerical simulations.

## 1. Introduction

The process of water vapor percolation and condensation is crucial in numerous applications, including subsurface contaminant remediation, (Bruining and Marchesin, 2006; Forsyth, 1993), management of geothermal reservoirs (Wang et al., 2021), concrete structures (Simon et al., 2007), nuclear safety (Chaparro and Saaltink, 2016), moisture management in textiles and building insulation (Fan et al., 2004; Huang et al., 2008), porous heat exchangers (Udell, 1985), steam-driven oil recovery (Chen et al., 2020), and gas-condensate reservoirs (Igwe et al., 2022) to mention but some. In these applications, especially those involving geomaterials, frequently some form of discontinuity, such as fractures, is present. These features can span a wide range of scales, from nanometers to kilometers. Despite its widespread occurrence, condensation in heterogeneous porous media has been less explored than other heat and mass transfer processes, such as evaporation (Nield et al., 2006).

Previous numerical studies provided insights into the driving mechanisms of condensation in homogeneous porous media without fractures or fracture networks. Sözen and Vafai (1990) numerically modeled the non-thermal equilibrium which condenses the flow of vapor

* Corresponding author at: The European Synchrotron Radiation Facility, 38043 Grenoble Cedex 9, France.
*E-mail address:* bratislav.lukic@esrf.fr (B. Lukić).

https://doi.org/10.1016/j.advwatres.2024.104872
Received 22 July 2024; Received in revised form 3 December 2024; Accepted 9 December 2024
Available online 16 December 2024

passing through a packed bed of ideal spheres. The authors examined the impact of pressure gradients, particle size, and the heat capacity of the solid phase on the condensation process applying a constant inlet pressure. They found that higher flow rates (*i.e.,* higher Reynolds numbers) enhance the condensation rate and the total condensate accumulation. A decrease in condensation was instead observed with an increasing particle size (*i.e.*, with higher permeability). However, this resulted in slower heat transfer between the solid and fluid phases and a faster advancement of the thermal penetration depth. Adding a non-condensable gas, (*e.g.,* dry air), to the injected water vapor was numerically shown to mitigate the risk of mobilization during steam-aided contamination removal (Kaslusky and Udell, 2002). This reduces the potential for contaminant accumulation and subsequent downward migration due to gravity. In this case, without considering the convective transport of condensed water, Ogniewicz and Tien (1981) numerically found that increasing the vapor velocity (*i.e.,* Peclet number) significantly enhances the rate of condensation. Zhang et al. (2007) reported that an increase in vapor temperature results in stronger condensation due to the rapid rise in vapor density. Additionally, increasing the bed particle diameter and porosity reduces the pressure difference and capillary forces. Crone et al. (2002a), Bergins et al. (2005) proposed analytical and numerical models for condensation during steam injection with high liquid content, pressure, and temperature, which were validated by experimental measurements. They observed a sharp condensation front with high water saturation propagating through the porous sample. A linear decrease in vapor breakthrough time was observed with an increase in the applied pressure difference. Class and Helmig (2002), Class et al. (2002) presented a numerical simulation for non-isothermal multiphase multicomponent processes in porous media, focusing on various remediation strategies for NAPL (non-aqueous phase liquids)-contaminated sites via injection of steam and air. They validated these models against temperature measurements in column experiments and showed that heterogeneity at larger scales can significantly influence system behavior and remediation efficiency, while small-scale heterogeneities have a minor impact. Igwe et al. (2022) conducted a pore-scale study using X-ray micro-computed tomography on the retrograde condensation of light alkanes in sandstones. They discovered that the nucleation process of condensation predominantly began in sharp corners of the pores, pore throats, and small pores, while the gas phase occupied the larger pores. These condensed nuclei then grew and coalesced, forming an interconnected network.

Condensation in isolated fractures or micro-channels, devoid of porous media, has also been studied in the literature. Wu and Cheng (2005), Hu and Chao (2007) investigated the flow patterns of condensed water in a smooth transparent micro-channel with trapezoidal cross-sections using video recording in the visible light domain. They demonstrated that, depending on the pressures and flow rates, the liquid film flow pattern on the channel walls can transit from smooth annular flow to slug-bubbly flow with large gas bubbles and liquid slugs. Specifically, Hu and Chao (2007) observed that with an increase in steam flow rate, the heat transfer rates also increased, which in turn enhanced the condensation rate and resulted in a higher pressure drop. Furthermore, experiments on the condensation of refrigerant coolant in parallel micro-channels showed that the higher mass velocity of the vapor reduces the occurrence of flow fluctuations since the increased interfacial shear stress helps maintain a stable and smooth annular flow regime (Kim et al., 2012). Higher flow rates also lead to more uniform temperature distribution along the channel, improving the overall efficiency of the condensation process (El Kadi et al., 2021).

Research on condensation in porous media has predominantly focused on homogeneous or layered heterogeneous cases. Except for a few examples summarized below, the investigation of condensation processes in heterogeneous porous media, particularly in fractured systems, remains largely underexplored in the literature. This gap is likely attributed to experimental challenges, with existing studies primarily concentrating on measuring the macroscopic steam leakage rate through damaged concrete (Simon et al., 2007; Medjigbodo et al., 2013, 2016). Simon et al. (2007) highlighted the influence of internal crack morphology on the leakage rate and overall concrete permeability. Medjigbodo et al. (2013, 2016) investigated the effects of saturation degree, mechanical loading, and fluid flow rate, focusing on long-term steady leakage rates. However, due to the influence of porous medium properties and imposed boundary conditions, they found out that achieving steady-state conditions is challenging. This indirectly suggests the transient nature of the condensation process for a considerable time after the start of vapor injection (Gupta et al., 2022). In a recent experimental work (Rabone et al., 2023), point-wise temperature measurements inside a concrete crack revealed fluctuating variations along the crack. These fluctuations were caused by blockages due to condensation and subsequent unblocking from the transport, absorption, or evaporation of moisture. The fluctuations were found to be more pronounced when the crack was narrower, the vapor-to-nitrogen ratio was higher, and the temperatures were more elevated.

Experimental measurement of vapor condensation in porous media remains challenging, primarily due to the difficulties in observing the condensation process and its interaction with heterogeneities as well as fractures *in-situ*. Previously, condensation has been measured using various experimental methods, such as visual inspection in a transparent cell (Hunt et al., 1988; Brouwers, 1996a), weighing (Fan et al., 2004; Qin et al., 2010; Fan et al., 2003) or visual inspection (Mcnamee, 2009) of the sample or parts of the sample during the condensation process, embedded measurement of relevant parameters such as pressure and temperature (Bergins et al., 2005), and 2D pointwise gamma-density measurements (Ochs, 2006). These methods are only applicable to a few points in time or space and cannot provide a complete time-evolving field of water accumulation within the sample. Additionally, some of these measure approaches tend to strongly affect the process itself, by introducing discontinuities or locally disturbing the porous matrix, and thus preventing accurate measurement (Dauti et al., 2020). In order to capture the detailed influence of microstructural variations, such as cracks, on condensation dynamics, full-field and *in-situ* measurements are necessary to obtain accurate data and gather a comprehensive understanding of vapor behavior in porous media. Neutron imaging is a powerful non-destructive tool that overcomes these limitations by providing a 3D visualization of the water content field in opaque porous samples due to its sensitivity to lighter elements like hydrogen (Tengattini et al., 2021; Kaestner et al., 2016). Recent advancements in cold neutron sources have made high spatio-temporal resolution possible for *operando* studies (Tötzke et al., 2019; Tengattini et al., 2021).

In previous studies, Lukić et al. (2021) employed neutron imaging for high-temporal measurements of vapor condensation in cracked concrete *in-situ*. This was achieved through high-speed neutron radiography, where the propagation of condensed water was observed using 2D projections. The focus of that work was mostly on the initial stages of the transient process, while the pressure as well as vapor content were not fully controlled during the process. Building on this work, Gupta et al. (2022) studied the effect of initial water saturation on vapor condensation in 3D using combined neutron and X-ray tomography. In dry concrete, they found competing water accumulation along the crack and into the matrix, while in saturated samples, water propagation along the crack was significantly faster than into the matrix. In fractured sandstones, a similar methodology was used by Nemati et al. (2023) to study water accumulation during vapor injection at a constant flow rate and vapor saturation, focusing on the interactions between the crack and porous matrix and interpreting the contributing mechanisms. The final condensed water distribution was found to result from two competing processes: condensation predominantly in the crack and diffusion towards the matrix due to the capillary effect as well as due to the pressure exerted by the vapor. Synchrotron microtomography at the pore scale revealed more water condensation

in areas with tighter pores, highlighting the significance of the capillary forces in the porous matrix.

The previous work on fractured sandstone presented a case study, providing a glimpse into water vapor condensation processes (Nemati et al., 2023). While it suggested the overall mechanisms of vapor condensation and water transport, it did not reveal the effects of important microstructural parameters in the system, such as the presence of cracks, flow rate, and porosity, which will be explored through various test cases in this study. These factors can play a influential role in the overall condensation process. Furthermore, the quantification of the water content field, which requires prior calibration experiments, was not performed in Nemati et al. (2023). Instead, the results were presented in terms of neutron transmission, with an uncertain correlation to water content. This limitation hindered the ability to validate and develop numerical benchmarks and to encourage future advancements in numerical modeling. In this work the calibration results performed by Nemati et al. (2024) were applied so as to extract the 3D water content in sandstone samples during constant flow rate vapor injection experiments. Consistency was observed between the overall evolving water content in the sample, as identified from the neutron tomography data, and the measured boundary condition in the experiments. A data bank of experiments was acquired using rapid neutron tomography to observe the fast condensation process *in-situ*, where each tomographic scan lasted for 30 seconds. The experiments performed in this work highlight the contribution of both microstructure and boundary conditions to the condensation processes. First, the effects of the fracture presence within the porous medium and the subsequent channeling effects were investigated by comparing samples with the same microstructural characteristics, with and without the presence of fracture along the injection path. Then, fractured samples with a markedly different matrix porosity were tested to observe the effect of matrix permeability and thus different capacities in absorbing condensed water. Finally, the effects of injection flow rate were investigated by performing repeated experiments on the same samples with different flow rates, after adequate drying between tests. The overall results show that the presence of a fracture combined with lower flow rates results in higher water accumulation in the porous matrix due to lower pressure-driven water migration. Additionally, the lower matrix porosity leads to higher water accumulation in the fracture, manifested in the form of patches of water and potential clogging sites, where water droplets coalesce, blocking further vapor passage locally.

The experimental methodology is discussed in the next section, which details the sample preparation, experimental setup, and neutron imaging configuration. Afterwards, the uncertainty in water content quantification is examined. Then, the results over the aformetion matrix of conditions are presented. The impact of the presence of a crack is discussed by comparing two samples of the same porosity and grain size, with and without an embedded fracture along the injection. Next two samples with a crack but with markedly different matrix porosities are examined to evaluate the effect of porosity. Finally, high and low porosity samples (with a crack) are tested, under repeated conditions, at a higher injection rate to explore the effect of vapor flow rate. The last section provides a discussion of the findings, comparing the presented experimental results to previous studies in the literature, and outlining the implications for practical applications and future research directions.

## 2. Materials and methods

### 2.1. Sample description

The sample size and cell were specifically designed to balance adequate neutron transmission from the cold neutron source (Tengattini et al., 2020) while maintaining a representative volume for observing local material responses and macroscopic processes during condensation in porous media. Samples of Fontainebleau sandstone, 40 mm in both height and diameter were used in this study. The choice of Fontainebleau sandstone was chosen because of its extensive presence in the literature, and its almost pure quartz structure without inter-grain contaminants (Bourbie and Zinszner, 1985), as well as its water-wet nature. Such material allows for focusing the study only on interactions between the matrix and cracks without potential chemical interactions among the different constituents during the process.

The samples were pre-fractured using an indirect tensile splitting test, *i.e.,* the Brazilian test. In this test, the cylindrical samples are placed horizontally between the plates compressed from the sides. This induces tensile stresses perpendicular to the applied load, causing the sample to split along a vertical diameter and initiate a single crack in the center of the circular cross-section of the sample, while leaving the rest of the sample intact. A feedback-controlled splitting test generates aperture-controlled cracks, with two LVDTs (Linear Variable Differential Transformers) monitoring crack opening displacement (COD). Wooden layers protect the specimen at loading points, and a closed-loop system adjusts the loading ram. The test stops at a target COD of 200 μm, ensuring the sample does not split into separate parts. More details about the Brazilian test is provided in Appendix.

### 2.2. Experimental setup

Fig. 1 depicts the experimental setup of the vapor injection and its installation within the neutron beamline. The experiment was performed on NeXT-Grenoble, the Neutron and X-ray Tomography instrument at the Institute Laue Langevin Grenoble (ILL) (Tengattini et al., 2020). The experiments were performed with a controllable vapor production system from 2 M Process, incorporating a controlled evaporator mixer delivery system (CEMLab) which controls vapor through aBronkhorst High-Tech (Boer, 1995), so as to deliver a precise mixture of Nitrogen gas and water vapor. The vapor was consistently injected into the sample using heat-controlled tubing, with all components preceding the vapor's entry into the sample being heated by heaters. The sample was secured within an aluminum cell (Al5083). To prevent vapor from escaping from the lateral surfaces and ensure a unidirectional flow upwards, the sides of the sample were sealed with PTFE tape and a neutron-transparent heat-shrinkable membrane (Geoshrink, ADTECH). The top of the cell was left open to allow the vapor to vent out at atmospheric pressure. The cell was equipped with temperature probes at both the inlet and outlet to complement the *in-situ* water content field obtained by neutron tomography, allowing for detailed insights into the evolving water distribution of the sample.

The temperature of the vapor at the sample's inlet is influenced by several factors including the temperature, vapor quality, and flow rate from outlet of the vapor production system, the heat loss, and the temperature of the heating tubes. Despite these multiple variables, a consistent inlet temperature for different experiments was achieved through careful boundary condition calibration, which facilitated the cross-comparison of the experiments. Given that heat loss from the cell and the initial temperature of the sample were consistent across all experiments, the outlet temperatures also remained reproducible. Fig. 2 illustrates the inlet and outlet temperatures of the vapor, with the standard deviations highlighted as error bands across the 6 reported experiments. The registered temperature variation across the experiments can be calculated to result in about 12% variability in the injected vapor volume. In order to avoid the bias deriving from these variations, the case-to-case comparison between experiments is only performed where the condensed water content is higher than twice the variability in the vapor delivered to the sample.

A sufficiently high vapor-to-air ratio, *i.e.,* more than 50% — higher than the vapor ratio of the saturated vapor across all temperature ranges throughout the experiments — has been chosen to ensure the delivery of saturated vapor. The imposed injection ensured a constant flow rate of nitrogen throughout the experiments. It should be noted that the injected vapor continuously loses heat because of the lower

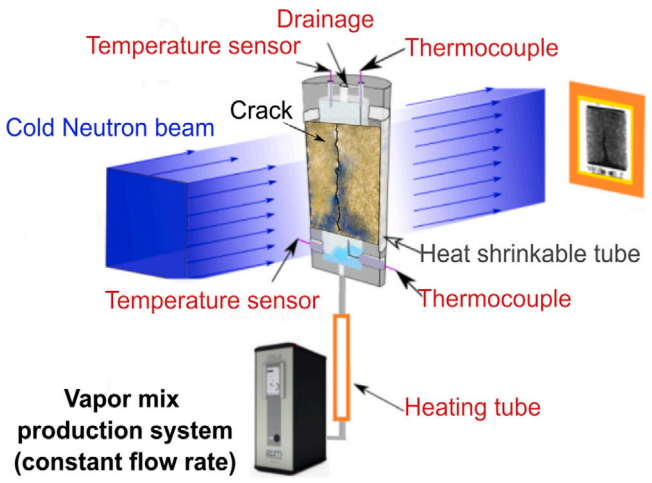


**Fig. 1.** Experimental setup for vapor injection at NeXT-Grenoble. The system delivers a heated nitrogen and water vapor mixture to a sample in a sealed aluminum cell, which allows unidirectional flow. The cell is vented at the top and equipped with temperature probes at the inlet and outlet, complemented by in-situ neutron tomography.

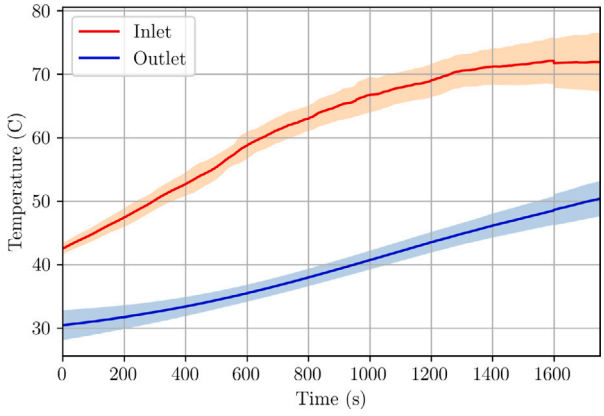


**Fig. 2.** Average inlet and outlet temperatures within all the reported experiments with reproducibility indicated by shaded colors representing standard deviation.

initial temperature of the sample with respect to the injected vapor. Consequently, any excess vapor that exceeds the saturated vapor content condenses before reaching the sample, ensuring the delivery of a saturated flow throughout the experiments as discussed in Nemati et al. (2023). The recorded inlet and outlet temperatures, together with the imposed injection parameters, can be used to calculate the theoretical total amount of condensed water in the samples. This is determined by the difference in the amount of water vapor between the inlet and the outlet:

$$\Sigma m_w = \int_0^t \dot{m}(W_{v,in} - W_{v,out})dt \tag{1}$$

where $\Sigma m_w$ is the total condensed water in the sample, $\dot{m}$ is the injection mass flow rate, $t$ is the duration of injection, and $W_{v,in}$ and $W_{v,out}$ make the mass ratio of vapor. The vapor mass ratios can in turn be obtained from the molar fraction of a gas, which is equal to the ratio between partial and total pressures:

$$x_v = \frac{p_v(T)}{p} \tag{2}$$

where $x_v$ is the molar fraction of vapor, $p$ is pressure (which is assumed to be equal to atmospheric one, given the relatively slow injection flow rate adopted in this study), and $p_v$ is the vapor pressure. Assuming the saturation condition of vapor, this vapor pressure is solely dependent on the temperature. $p_v$ can therefore be determined either through thermodynamic tables or by using empirical correlations such as the Antoine equation, both of which provide comparable results.

This study focuses on six vapor injection experiments designed to investigate different factors affecting the process of water vapor condensation in porous media. These experiments are summarized in Table 1 and are analyzed in case-to-case comparisons, each of which focuses on the effects of the presence of fracture, matrix porosity, and vapor flow rate, respectively. A sixth experiment, reported to investigate the repeatability of the process and discussed in the Appendix, involved two similar samples tested under identical conditions, with results indicating good repeatability.

Two samples from high and low porosity blocks of Fontainebleau sandstones were scanned by synchrotron microtomography at the ID19 beamline of the European Synchrotron Radiation Facility (ESRF), with a pixel size of 6.5 μm. The sample was positioned 1 m from the detector to take advantage of the in-line phase contrast modality, leveraging the high coherence of the X-ray source starting 145 m away. The resulting enhanced contrast at grain boundaries still preserves the geometry of the sample, which is used to study the detailed microstructure and pore distribution. The analysis of the microtomography shows that the mean porosities of the high and low porosity blocks are $8.8 \pm 0.8\%$ and $3.2 \pm 0.2\%$, respectively. Gas permeability tests indicate corresponding permeabilities of $3.75 \times 10^{-13}$ and $1.7 \times 10^{-14}$ $m^2$ for the high and low porosity samples, respectively.

### 2.3. Neutron imaging

Neutron imaging was employed to take advantage of the high sensitivity of neutrons to hydrogen, and therefore water, and notably to quantify the 3D condensation process over time. A collimated cold neutron source, with a peak wavelength at 2.7 Åwas directed at the sample (at the NeXT-Grenoble instrument). The beam interacted with the sample, and the transmitted fraction was captured by a powder-based scintillator (100 μm thick $^6$LiF/ZnS, with a 0.5 mm Al substrate), which produced a projection image in the visible light spectrum. The resulting image was conveyed optically to an sCMOS sensor (Orca-Flash 4.0 V2, Hamamatsu) using a 50 mm f./1.2 Canon lens (Tengattini et al., 2020). The sample was placed as close to the neutron detector as possible (l=40 mm, which was constrained by the cell geometry). A 35m pinhole, placed at 11 m, yielded a neutron penumbra around 130μm, which was not the limiting factor in this study as detailed below.

To find an optimum between acquisition speed and resolution and maintain an acceptable signal-to-noise ratio, the camera was binned 4 × 4, yielding a 160 μm virtual pixel size, and a 100 μm ZnS/$^6$LiF scintillator was employed. This reduced the exposure time to 0.02 s per radiography.

The rapid tomographies consisted of 500 projections, each the result of the average of 3 radiographies per angular position, captured over a continuous 0–180°rotation, followed by a fast reverse rotation (without imaging) to reset for the next scan, resulting in tomographies that lasted 30 s. The sets of projections were reconstructed using filtered back projection and Ram-Lak filter kernel in the ASTRA toolbox (van Aarle et al., 2016). It was then followed by a 3D Gaussian filter (standard deviation of 1.5 voxels) to smooth the data and mitigate noise unavoidable with the low exposure time. A more detailed description of the imaging system is available in Nemati et al. (2023, 2024), Tengattini et al. (2020).

The Beer–Lambert Law is conventionally used to model the absorbance of neutrons by a substance, assuming that the transmission of neutrons ($T$) is proportional to the path length through the sample ($l$) through the relation:

$$T = \exp\left(-\int_0^l \mu(l)dl\right) \tag{3}$$

**Table 1**
Summary of vapor injection experiments. The vapor flow rate is reported in liters per minute in ambient pressure.

| Sample | Fracture | Matrix Porosity | Flow rate (lpm) | Remarks |
|---|---|---|---|---|
| Exp-01 | No | High | 0.22 | – |
| Exp-02 | Yes | High | 0.22 | – |
| Exp-03 | Yes | Low | 0.22 | – |
| Exp-04 | Yes | High | 0.3 | Same sample as Exp-02 |
| Exp-05 | Yes | Low | 0.3 | Same sample as Exp-03 |
| Exp-06 | Yes | Low | 0.3 | Same condition as Exp-05 |

where $\mu(l)$ is the macroscopic linear attenuation coefficient of the sample constituents along the beam path. The transmission is conventionally normalized as:

$$T(t) = \frac{I(t) - \bar{I}_d}{\hat{I}_f - \bar{I}_d} \tag{4}$$

where $I(t)$ is the measured pixel intensity when the beam is transmitted through the sample, $\hat{I}_f$ is the beam without the sample (open beam image), and $\bar{I}_d$ is the background noise of the camera (dark field image) to account for any non-uniformity of the neutron beam and detection system.

The reconstructed series of tomographies provide a 4D (3D + time) field of attenuation coefficients which can be here expressed as a function of its constituents:

$$\mu = \sum_{i=1}^{N} \mu_i \phi_i = \mu_s \phi_s + \mu_w \phi_w \tag{5}$$

where $\phi_s$ and $\phi_w$ are the volume fractions of the solid and condensed water phase, and $\mu_s$ and $\mu_w$ are their corresponding macroscopic attenuation coefficients. Water vapor and nitrogen gas may attenuate the neutron beam as well, but due to their significantly lower density, their contribution to the absorption contrast can be considered negligible in the first approximation. The initial dry scans ($\mu_{dry}$) are used to isolate the solid phase from the wet scans ($\mu_{wet}$) providing a direct measurement of the water content:

$$\phi_w = \frac{\mu_{wet} - \mu_{dry}}{\mu_w} \tag{6}$$

However, in practical scenarios, the Beer–Lambert law may not be applicable due to the contribution of neutron scattering (notably, from interactions with elements with large incoherent scattering cross-sections such as hydrogen). In addition, the use of polychromatic radiation neutron sources results in a wavelength-dependent attenuation coefficient, which can lead to additional beam hardening effects (Tremsin et al., 2019). These contributions, if not accounted for, may question the validity of the use of Eqs. (3)–(6) due to deviations and non-linearities in the assumptions made by the Beer–Lambert law. In a previous study (Nemati et al., 2024), the impacts of scattering and beam hardening of water were investigated at NeXT, with a specific focus on the effects of water content measurements, as deduced from calibration experiments on reference samples (phantoms). Results showed that, for water thicknesses in the range of [0, 4] mm along the beam direction, the deviation from the Beer–Lambert law is negligible, and scattering as well as beam hardening contribution can be taken into account simply by selecting an appropriate water attenuation coefficient. For the current experiments, with the maximum water thickness of 4 mm and the sample-to-detector distance of 4 cm, the attenuation coefficient for water is adopted to be $0.403 \pm 0.052$ mm$^{-1}$ based on the calibration experiments in Nemati et al. (2024).

## 3. Results

The results are structured in the following four subsections: first, the estimate of the uncertainty of the water content measurement is quantified. Second, the impact of a crack's presence is explored by comparing a cracked sample with a similar, but crack-free sample. Subsequently, the influence of matrix porosity is examined by comparing two cracked samples with differing porosities. Finally, the effects of varying vapor injection flow rates are investigated using a cracked sample under two flow rate conditions.

### 3.1. Water quantification

The uncertainty in measuring water content with neutron imaging in our work is chiefly determined by a combination of four biases. The most notable are (1) the contribution of (incoherent) scattering of neutrons, notably from hydrogen atoms, (2) the polychromatic nature of the beam which results in difficulty in calculating a reference value of the water attenuation coefficient; (3) the noise contributions impacting the measurement of the overall sample attenuation field and (4) the biases related to the reconstruction algorithms themselves.

In this work, the aforementioned uncertainties in water quantification are estimated as follows. First, the uncertainty on the attenuation coefficient from scattering and polychromacity of water is accounted for based on the calibration experiments reported in Nemati et al. (2024). Second, the source of uncertainty arising from the overall signal-to-noise ratio (*i.e*, SNR=17), which mostly results from short exposure time (made, in turn, necessary by the high intrinsic speed of the process) is estimated from multiple dry scans prior to the injection. Due to this inherent noise, these scans are not identical, showing some level of variation. The standard deviation of the subsequent residuals of these scans is adopted as the measure of the uncertainty arising from overall noise components and accounted for in the error estimation in the following steps. Finally, the uncertainty introduced during the reconstruction of the attenuation field is evaluated through simulated imaging experiments. A 3D pore-scale scan obtained using synchrotron X-ray microtomography at the ID19 beamline of the European Synchrotron Radiation Facility (ESRF) with 6.5 µm pixel size is used as a base for microstructure segmentation. The obtained field of pore space and the matrix are used to create a binary 3D volume of a sample. Various values of water content are reproduced by randomly adding water to the pore space. Then, the simulated volume is used to obtain the same number of synthetic projections as in the experiment. This is calculated using the Radon transformation and binning them to a pixel size comparable to the one of the rapid neutron tomographies. Finally, synthetic reconstructions were obtained using the same algorithm as for the analysis of neutron data. The local water content of the resulting reconstructed volumes is compared to the arbitrarily added water content of the original model. The uncertainty of the overall reconstruction algorithm and the partial volume effect are thus determined. The final estimate of the uncertainty of water content is obtained as the square root sum of the squares of these sources of uncertainty, with the primary contribution arising from noise due to the short exposure time.

Fig. 3 shows the average water content obtained from neutron tomography data in tested samples with the estimated uncertainty reported as error bars over the entire in-situ test. For comparison, the estimate of the total amount of the condensed water using the inlet and outlet temperature (Eq. (1)) is shown for each experiment, with the corresponding uncertainty, based on the precision of the temperature probes, expressed as error bands. In all the experiments, the water content calculated from the boundary conditions seems in agreement with the values obtained from rapid neutron tomography up to the breakthrough point (*i.e.,* the instant when condensation is visible at the sample face opposite to the injection).

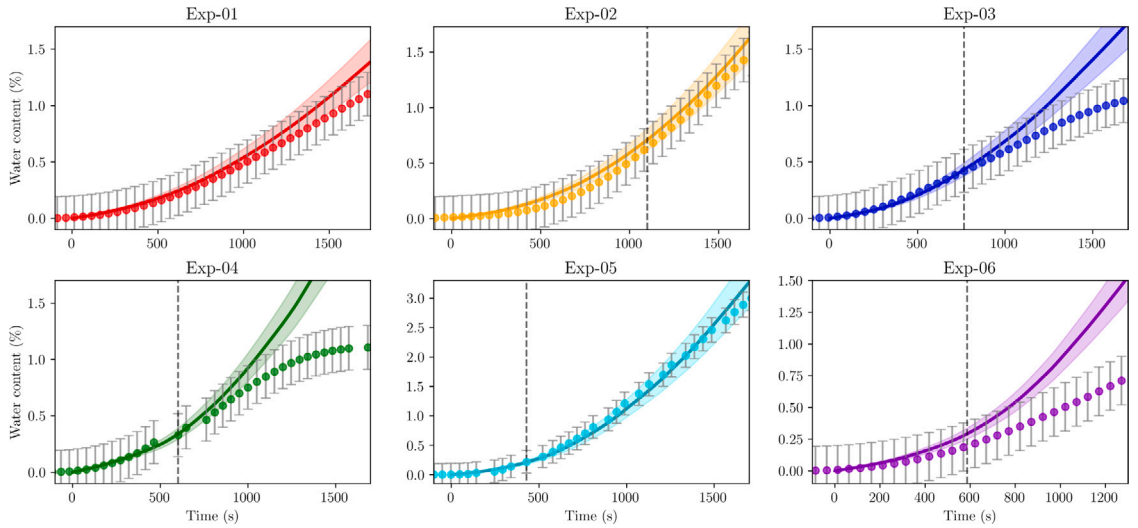


**Fig. 3.** The overall water content in the sample over time, based on the difference in the inlet and outlet humidity (solid line) and rapid neutron tomographies (points), with the corresponding error bands and error bars. Vertical dashed lines show the instant of the breakthrough of condensed water.

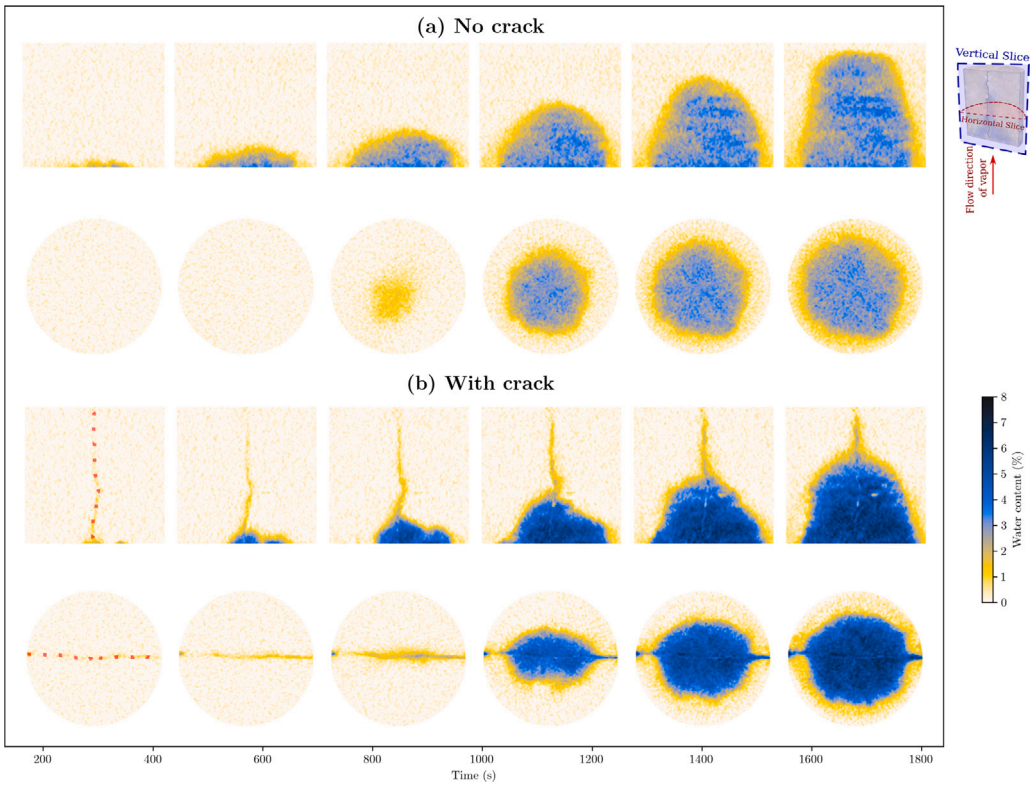


**Fig. 4.** Comparison of water content along a vertical and horizontal slice at different stages of the injection process for samples (a) without (*Exp-01*) and (b) with the induced crack (*Exp-02*). Dotted red lines on the initial slices show the position of the fracture.

### 3.2. Effect of fracture presence

To assess the impact of the presence of a fracture within the porous matrix, two samples of the same porosity are tested under comparable boundary conditions but adopting a sample with (*Exp-02*) and a sample without (*Exp-01*) fracture pre-developed through the Brazilian splitting test (as detailed in Section 2.1).

Fig. 4 shows the corresponding condensed water content for the two samples, along a vertical and a horizontal slice, compared at various times throughout the injection process.

In the case of the sample without a fracture, the condensed water begins to accumulate from the bottom of the sample (*i.e.,* the inlet) and gradually propagates towards the top of the sample (*i.e.,* the outlet). With the constantly rising injection temperature (as shown in Fig. 2), more condensed water is observed to accumulate also behind the main water front. This continuous temperature increase, as well as capillary diffusion of the water front, made possible by the sufficient time and the slow injection rate, prevents the formation of a sharp front, which was for example observed in Brouwers (1996b), Crone et al. (2002b). However, the rising water in the sample is observed to plateau over time, as shown in Fig. 5a, in particular during the late stages of

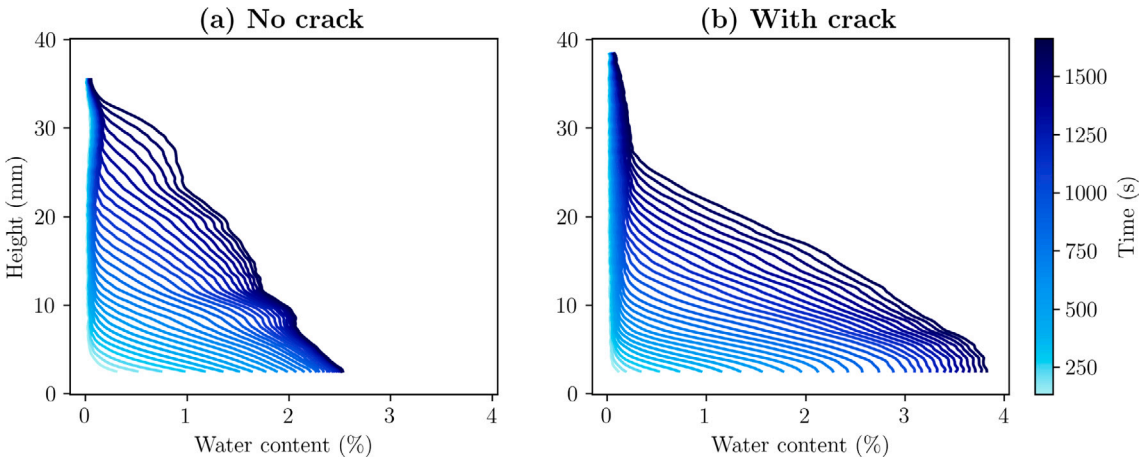


**Fig. 5.** Average water content along the height of the sample at various times for samples (a) without (*Exp-01*) and (b) with the induced crack (*Exp-02*). The water content is averaged over the cross-section of the sample.

injection. This indicates that the water content surpasses the critical saturation point, allowing water to flow due to the pressure buildup from the injection flow applied at the inlet.

Conversely, in the sample with a fracture, the condensation begins in the fracture itself. The condensation front obtained within the fracture area reaches the top of the sample in as few as ~600 s, exhibiting a much shorter breakthrough time than the homogeneous counterpart (whose breakthrough is not observed over a comparable injection period). The front advances slower in the porous matrix and propagates both along sample height and perpendicular to the fracture (*i.e.,* overall obliquely) towards the sample boundaries. Such propagation is attributed to the two conjugate capillary acts: one from the condensation of vapor in the crack surface, and one from the condensation taking place in the bottom of the sample both of which propagate by capillarity and pressure buildup of the vapor (Nemati et al., 2023).

An important observation that can be made from Fig. 4 is the markedly higher condensed overall water content in the sample with a fracture. Figs. 4 and 5 also demonstrate that for a given height, the fractured sample eventually retains more water within its porous matrix compared to the uncracked sample, despite similar injection flow rates and matrix porosity. Part of the higher water accumulation in the fractured sample can be attributed to its slightly higher porosity ($9.5 \pm 1\%$ vs $8.1 \pm 0.8\%$). However, the difference in water content indicates a much larger disparity (over 35%) than what the porosity difference alone would suggest. This difference can be likely due to the fact that the vapor pressure is applied primarily within the crack (rather than the porous matrix) in the cracked sample, where vapor tends to follow preferential pathways along the crack. This allows water to accumulate in the porous matrix without being transported further away by the vapor. In contrast, in the uncracked sample, the porous matrix serves as the sole pathway for vapor, thus the injection pressure prevents excessive water accumulation in the matrix. Alternatively, the presence of a fracture results in a significantly lower inlet pressure to maintain a similar flow rate. When the pressure exerted by the injected vapor decreases, the gas's ability to transport condensed water diminishes, leading to increased water accumulation in the matrix. Another factor contributing to increased water accumulation in the fractured sample could be the presence of microfractures perpendicular to the fracture surface, extending into the porous matrix. These microfractures, resulting from the splitting test, may facilitate the transfer of water from the main fracture into the surrounding matrix. The higher water accumulation in the fractured sample leads to a more delayed propagation of water in the porous matrix, as shown in Fig. 6. This figure compares water fronts in both samples with and without the

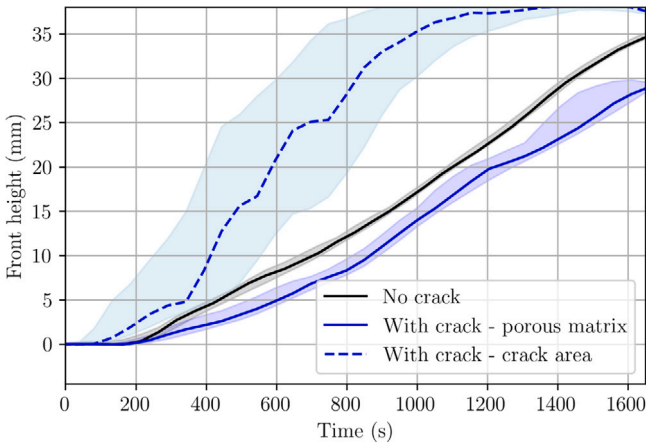


**Fig. 6.** The advancement of the water front in the porous matrix over time along the height of the samples with (*Exp-02*) and without (*Exp-01*) crack. The blue dashed line shows the water front in the area near the crack in the latter sample.

fracture. Here, the front threshold is defined as the 0.38% overall condensed water content (radially averaged over the height), equivalent to two times the uncertainty of the water content (*i.e.,* noise limit). Given the similar vapor flow rates and, consequently, the comparable overall amount of total condensation in both experiments, the water front in the porous matrix propagates slower in the fractured sample due to the higher water content it accumulates. As previously discussed, the initial propagation of the water front near the crack in the fractured sample occurs sooner and moves faster compared to the propagation in the porous matrix of both samples. Since the spatial resolution of the tomography scans is not enough to accurately segment the crack, the advancement of the water front is demonstrated in an area close to the crack, where we are certain the crack is located.

### 3.3. *Effect of matrix porosity*

The impact of matrix porosity (and thus, permeability) has been investigated by testing two samples of different porosities, both containing the pre-inserted fracture (*Exp-02* vs *Exp-03*). Fig. 7 displays the distribution of water content across vertical and horizontal sections during different phases of the injection process in high and low porosity samples. The saturation process in the crack in the low porosity sample occurs in two distinct stages. Initially, the saturation process in the low porosity sample resembles that of the high porosity sample, where a

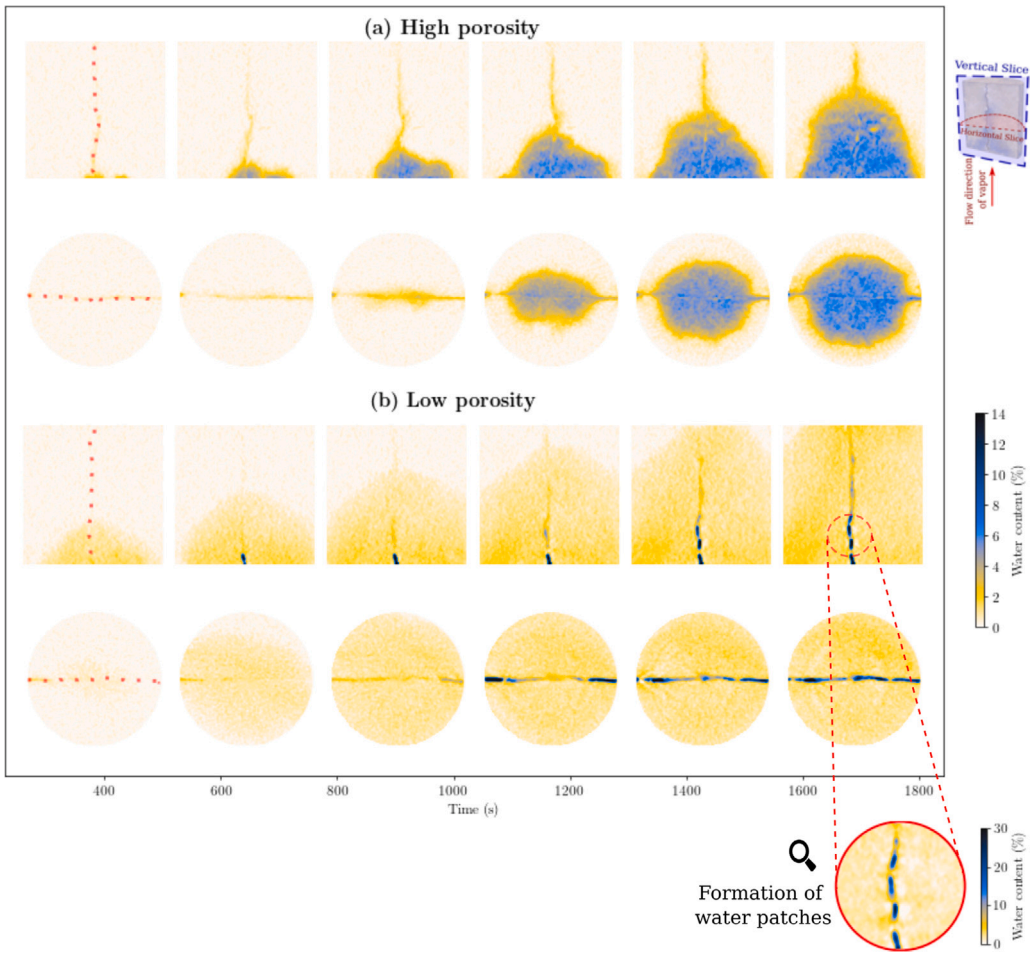


**Fig. 7.** Comparison of water content along a vertical and horizontal slice at different stages of the injection process for samples with (a) high (*Exp-02*) and (b) low porosities (*Exp-03*). The inset shows the patches of condensation in the fracture and their high water content. Dotted red lines on the initial slices show the position of the fracture.

low water content in the crack accumulates soon after injection begins, showing that the condensed water is immediately propagating towards the outlet. As the test progresses and the porous matrix becomes more saturated with condensed water, the porous matrix reaches a point where it can no longer absorb additional water. This trapped water, then, accumulates within the fracture, marking the second stage of fracture saturation. This stage is characterized by higher water content and gradual propagation of the saturation front within the crack.

The advancement of the water front in the matrix of the samples with high and low porosities is computed in Fig. 8. Since the low porosity sample can hold less water, the condensed water spreads faster and reaches the top of the sample more rapidly. The water front does not reach the top of the porous matrix in the higher porosity sample throughout the injection process (Fig. 8), leaving some parts of the sample dry. This is in contrast to the low porosity sample, where the water front reaches the top within 1200 s. At this point, the water content in the matrix becomes relatively stable and steady. Faster spreading in the low-porosity sample is driven by stronger capillary effects, which dominate over the reduced permeability associated with smaller pore sizes.

In Fig. 9, the average water contents as a function of the height of the samples at various times are compared for the samples with high and low porosities. It highlights the impact of the matrix porosity on the water content evolution in the porous matrix (shown in green) and the area near the crack (in red). The data reveals significant differences between the two samples. The sample with higher porosity shows a higher overall capacity to absorb water, as expected. The water content plots in the porous matrix (Fig. 9a, b) illustrate that, while the water

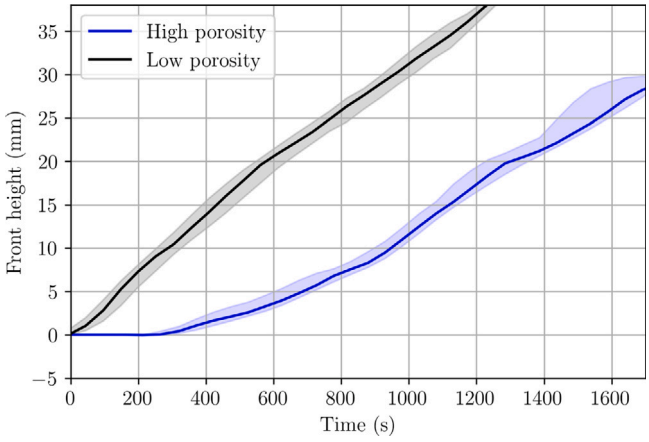


**Fig. 8.** The advancement of the water front in the porous matrix over time along the height of the samples with high (*Exp-02*, top) and low porosities (*Exp-03*), bottom.

content in the matrix of the less porous sample is beginning to stabilize and plateau, the water content in the more porous sample continues to rise. However, within the cracks of both samples (Fig. 9c, d), the water content is constantly increasing, but the increase is more pronounced in the sample with lower porosity. Initially, the water content in the crack of the low porosity sample increases at a steady rate, similar to that observed in the high porosity sample. However, once the capacity of the

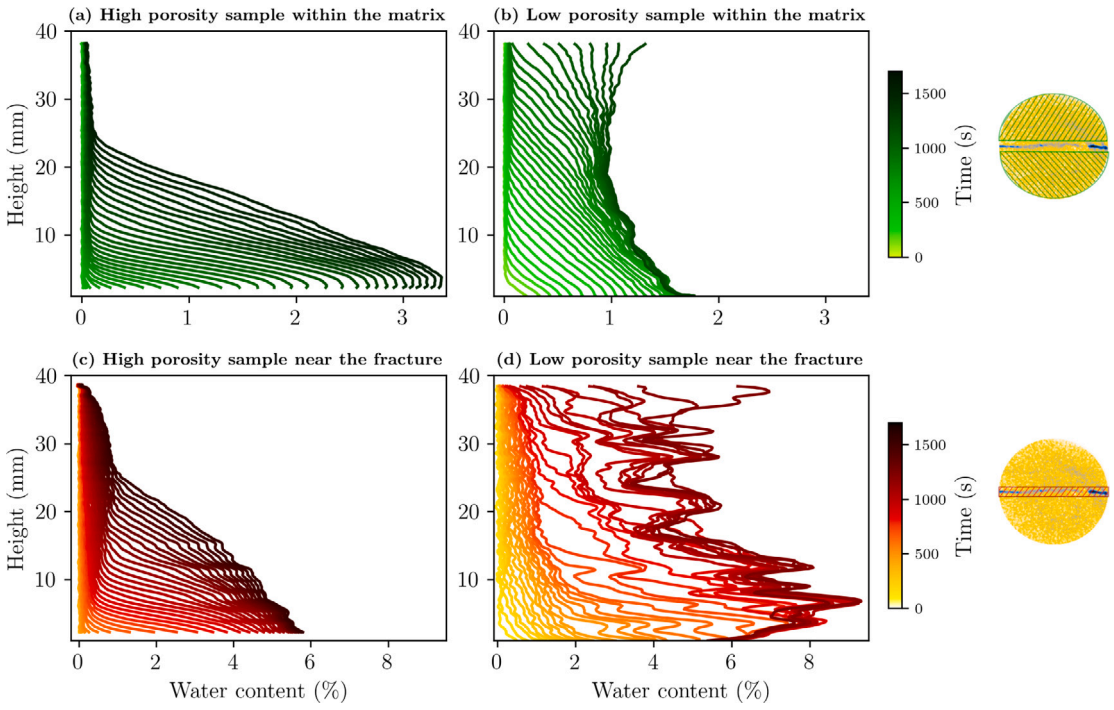


**Fig. 9.** Average water content as a function of the sample height at various times for samples with (a and c) high (*Exp-02*) and (b and d) low porosity (*Exp-03*), over the porous matrix (in green) and the area near the crack (in red).

matrix to absorb water is approached, a new pattern in the distribution of water within the crack begins to emerge. This is characterized by the formation of distinct fluctuations along the sample height, which are likely influenced by the formation of local water patches. Remarkably, localized water contents as high as 30% can be observed in the low porosity sample. Nemati et al. (2023) demonstrated that condensed water in the crack tends to accumulate in smaller crack openings, as evidenced by multi-modal image analysis of neutron imaging data (for water visualization) and X-ray tomographies (for crack morphology analysis). The formation of patches of water after the saturation of the porous matrix shares similarities with condensation in non-porous channels, where the flow is marked by irregular, intermittent flow dynamics with gas bubbles interspersed by pockets of liquid (Kim et al., 2012; El Kadi et al., 2021).

### 3.4. Effect of vapor injection flow rate

#### 3.4.1. Effect of flow rate on a high porosity sample

In this section, the effect of the injection flow rate of vapor is investigated in the high porosity sample with pre-formed fracture. Two flow rates were used, namely 0.22 liters per minute and 0.3 liters per minute (*Exp-02* vs *Exp-04*). To ensure similar conditions, drying was performed before both tests, by placing in an oven at 70,°Celsius for 24 h. More vapor is condensed, perhaps unsurprisingly, in the case with a higher injection flow rate where the advancement of the wetting front is faster and spreads further both horizontally and vertically. This is because more vapor is injected into the sample, and consequently, more condensation is observed. To isolate the effects of the different vapor injection rates, Fig. 10 illustrates the evolution of condensed water content as a function of the cumulative amount of injected vapor. The data show that higher local water content values are accumulated at the slower flow rate experiment when compared with similar amounts of cumulative injected vapor. This can be attributed to the fact that at higher flow rates, the pressure of the injected vapor is higher and is able to push the condensed water further than at lower flow rates. This leads to overall lower water content in the porous medium.

The broader spread of the water front for the higher flow rate is clearly visible in Fig. 11, which compares the front height in the porous matrix (excluding the crack area) for the two flow rates. Despite being plotted as a function of the cumulative injected vapor, the front propagates faster at the higher flow rate, illustrating the significant role of pressure-driven water migration in this scenario.

The higher water content and the lower spreading of the wetting front can be better discerned in Fig. 12, where the water content is plotted along a line that passes through the central axis and crosses the center of the crack perpendicularly. A key observation here is the evolving water content around the crack area. A peak in water content is observed in this area during the early stages of injection. However, as the injection continues, the water content in the surrounding matrix surpasses that in the crack, leading to a noticeable reduction in the water content in the fracture. This effect is more pronounced for the case of higher flow rates, as illustrated in Fig. 12b, and further evidenced by Fig. 10b. A comparable finding was observed in the case study conducted by Nemati et al. (2023), where the crack was segmented from the X-ray tomography data and found to hold less water than the porous matrix near it (as computed from in-situ neutron tomography) in the later stages of injection.

The crack serves as the primary conduit for vapor flow throughout the injection, leading to initial condensation within the crack itself. This condensed water is then gradually absorbed by the porous matrix through capillary action. In this case, where the matrix has sufficient absorptive capacity, it continues to absorb water throughout the injection process. Due to the preference of the matrix to retain water and the pressure exerted by the vapor in the crack, which encourages the water to disperse, the water content within the crack decreases compared to that of the surrounding porous matrix. As the water content in the matrix increases, the lower capillary forces enhance the mobility of the water, resulting in an even more pronounced decrease in the moisture accumulation in the fracture over time. In the case with higher flowrate, higher pressure buildup within the fracture leads to a more significant reduction in water content in the fracture area, compared to that within the porous matrix.

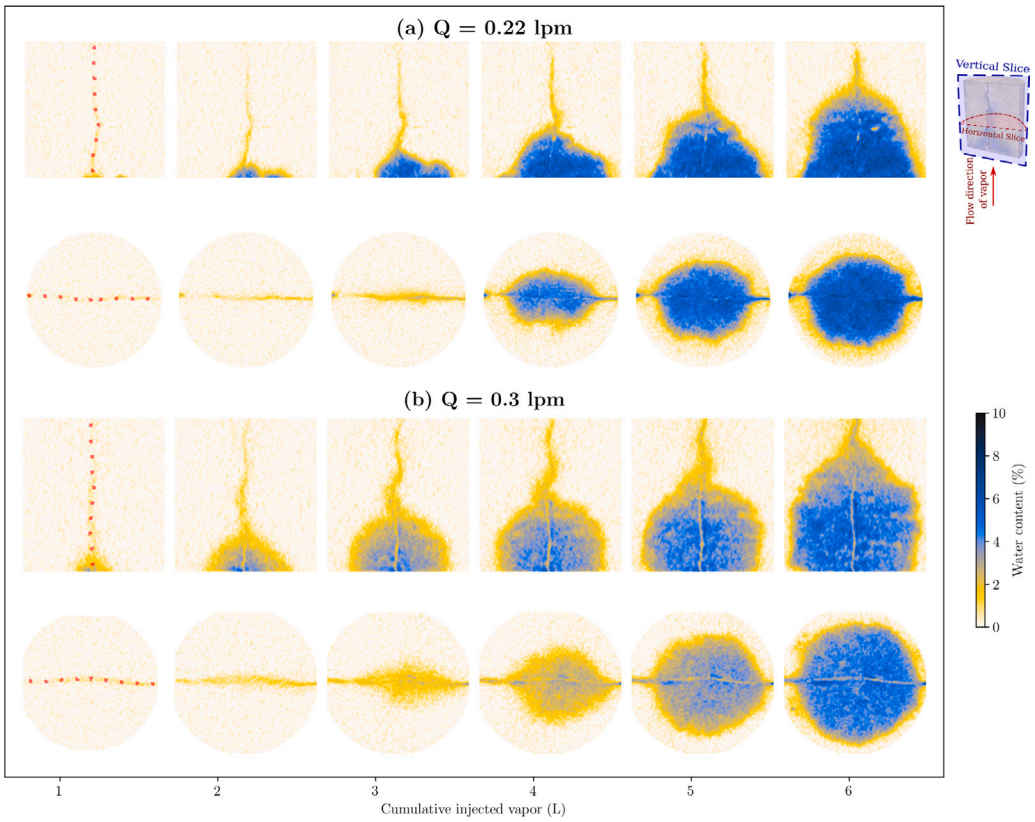


**Fig. 10.** Comparison of water content along a vertical and a horizontal slice at different stages of the injection process for the high porosity sample at (a) low flow rate (0.22 liters per minute, *Exp-02*) and (b) high flow rate (0.3 liters per minute, *Exp-04*). Dotted red lines on the initial slices show the position of the fracture.

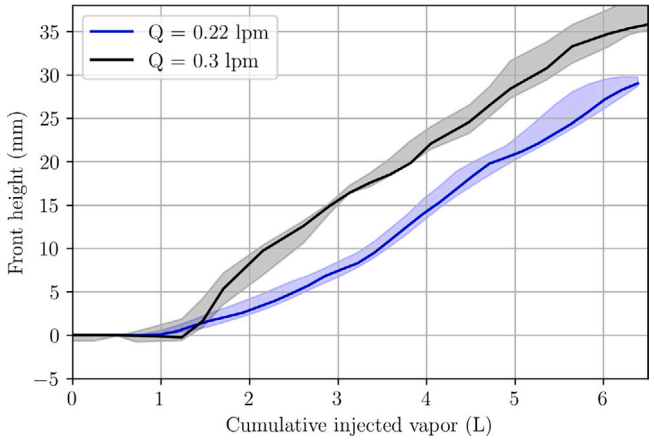


**Fig. 11.** The advancement of the water front in the porous matrix over time along the height of the sample during low (*Exp-02*) and high vapor injection rates (*Exp-04*).

### *3.4.2. Effect of flow rate on low porosity sample*

The experiments with low and high flow rates were also conducted on a low porosity sample (low flow rate: *Exp-03* and high flow rate: *Exp-05*). Similarly to the high porosity case, faster wetting front propagation is unsurprisingly observed for the high flow rate experiment. However, when comparing the two injection rates over the same cumulative injected vapor content (Fig. 13), the faster propagation of the water front in the higher flow rate is less pronounced compared to the high porosity sample. This can be attributed to the lower matrix permeability which prevents the transport of the condensed water in the matrix.

Fig. 14 illustrates the evolution of the average water content along the height of the samples. The water content in the porous matrix (Fig. 14a and b) appears to have stabilized in the lower half for both cases at the end of injection, indicating that the porous matrix reached its maximum capacity for water absorption. However, the water content appears to be slightly higher in the low flow rate experiment. In the crack area (red curves), initially, a steady increase is observed, similar to the high porosity cases. However, after the saturation of the porous matrix, the water content in the crack rises rapidly, and an instability, likely linked to patches of water forming, appears, similarly to the case of the low porosity sample in Section 3.3. The results show that lower flow rates lead to greater formation of these water patches, suggesting that at higher flow rates, the pressure-driven transport disperses the accumulated water more effectively towards the matrix or the outlet. Furthermore, at the higher flow rate, the patches of condensed water in the fracture exhibit rapid transitions from one location to another which occurs in a fraction of a second, as revealed when inspecting individual radiographs.

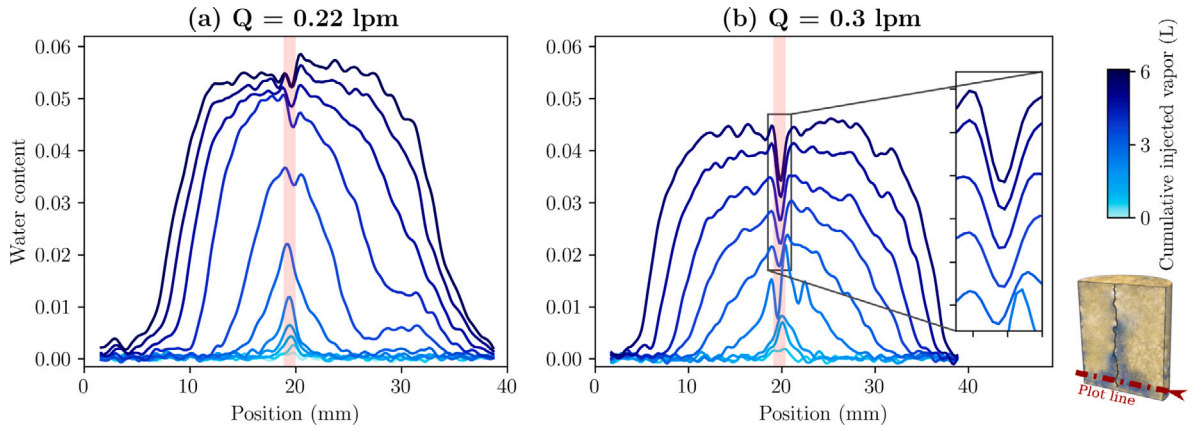


**Fig. 12.** Water content distribution plotted along a central line intersecting the crack perpendicularly over various times for (a) low flow rate (0.22 liters per minute, *Exp-02*) and (b) high flow rate (0.3 liters per minute, *Exp-04*).

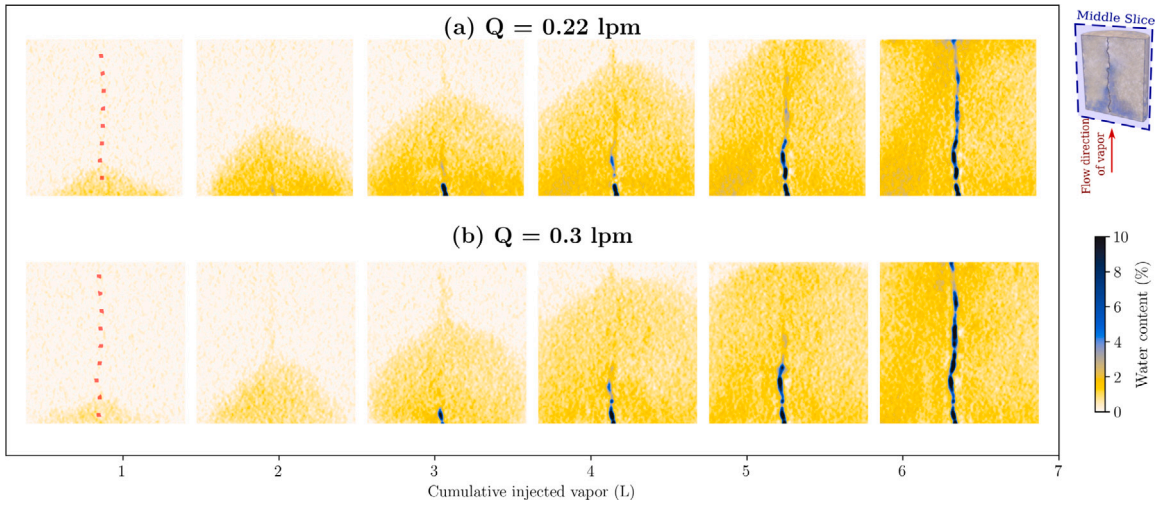


**Fig. 13.** Comparison of water content along the middle vertical slice at different stages of the injection process for low porosity sample at (a) low flow rate (0.22 liters per minute, *Exp-03*) and (b) high flow rate (0.3 liters per minute, *Exp-05*). Dotted red lines on the initial slices show the position of the fracture.

## 4. Discussion

Condensation starts from the inlet side of the sample and percolates towards the matrix area. Due to the constant increase in the temperature of the delivered vapor and of the matrix itself, the rate of condensed water content in the sample gradually increases until stabilization. The stabilization of the overall water content in the sample without a fracture is attributed to the equilibrium in the transport of water by the pressure exerted by the vapor and the capillary absorption of the matrix. It is made possible by the increased mobility of water within the matrix, resulting from achieving high water saturations in the sample. In comparison, a sample with a fracture along the injection direction shows the inception of condensed water in the fracture itself from the very early stages of injection. This indicates that the fracture acts as the preferential pathway for the vapor. In the later stages of the injection process, the condensed water in the fracture starts to be progressively absorbed by the porous matrix due to the capillary action. This was shown to be evidenced by the tendency of the porous matrix to accumulate condensed water in areas where tighter pores are present (Igwe et al., 2022; Nemati et al., 2023). The saturation of the matrix continues until the entire matrix domain is saturated, after which the fracture begins to accumulate more water. This behavior resembles the imbibition process described by Rüdiger et al. (2022), where the fracture initially saturates quickly, slows down as the matrix absorbs water, and finally, once the matrix is saturated, transitions back to being fracture-dominated. The propagation of the water front into the porous matrix for the fractured sample is slower than the sample without a fracture, but more water accumulates in its porous matrix. Since a significant portion of the injected vapor passes through the fracture, less pressure is applied to the matrix allowing for more accumulation of condensed water. In this regard, another mechanism for condensed water transport is the condensation near the inlet of the sample where the corresponding capillary absorption takes effect leading to further transport within the porous matrix.

The impact of matrix porosity was investigated by conducting experiments with two fractured samples of different matrix porosities. More water accumulated in the sample with higher porosity. Since the flow rate was kept constant for both experiments, it follows that the propagation of the water front is faster in the lower porosity sample. Initially, the behavior of water accumulation in the fracture, relative to the matrix, is similar between the two samples. In both sample cases, the fracture becomes partially saturated early, followed by the absorption of water by the porous matrix. Since the water absorption capacity of the matrix with lower porosity is lower, it saturates faster, causing the condensed water in the crack to accumulate in this case in a patchy structure. The formation of these patches is similar to the case condensation in a microchannel with impermeable walls (El Kadi et al., 2021). Previous experiments on fractured porous media show that water patches (wetting phase) in the crack tend to accumulate where the crack aperture is smaller due to capillary action (Bertels

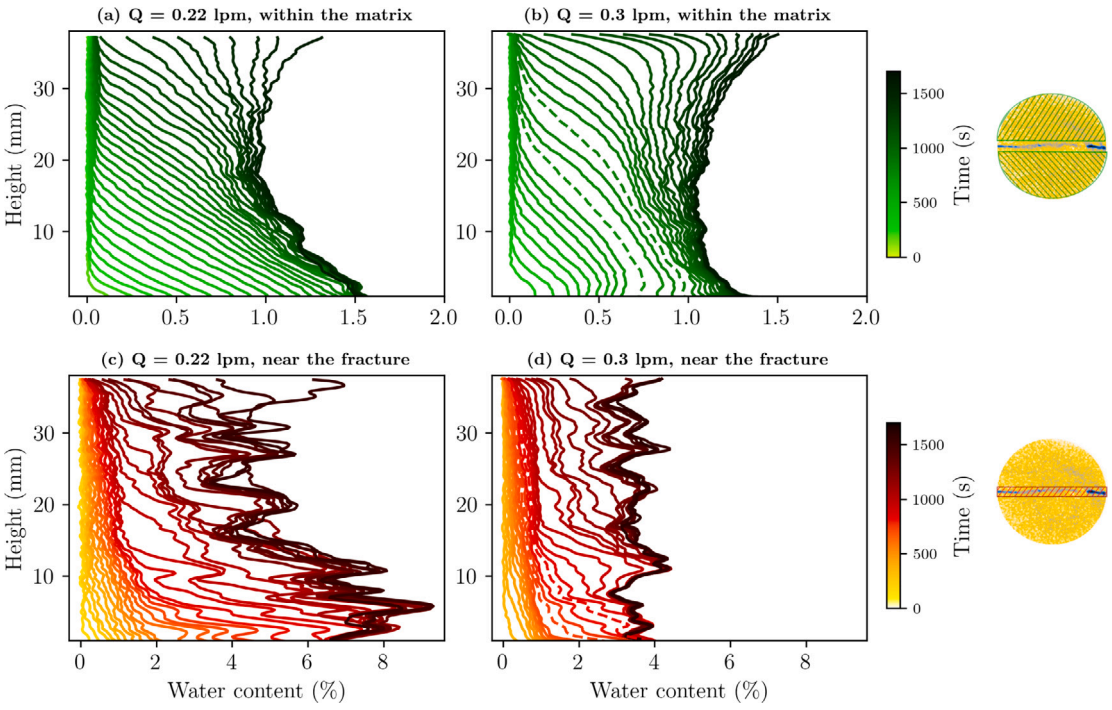


**Fig. 14.** Average water content as a function of sample height at various times for (a and c) low flow rate (Q=0.22 lpm) and (b and d) high flow rate (Q=0.3 lpm), over the porous matrix (in green) and the area near the crack (in red). Some tomographies are missing due to technical problems which are interpolated in dashed lines.

et al., 2001; Karpyn et al., 2007). It has also been shown that surface tension is the dominant force governing condensation and two-phase flow in microchannels, shifting the flow patterns to intermittent slug bubble flow in narrow channels, unlike the stratified or annular flow observed in larger channels (Chen et al., 2008). It should be noted that the thermal contribution caused by the microstructural differences between the two samples in the porous matrix is expected to be low, as thermal equilibrium in both cases between the fluid and matrix is maintained (due to the low porosity and small grain size of both samples as discussed in Nemati et al., 2023).

Finally, fractured samples of both high and low matrix porosity were tested under two different flow rates to explore the impact of vapor pressure. Unsurprisingly, with a higher injection rate, more water content was observed, and the wetting front propagated faster. However, when comparing water propagation for the same amount of cumulative injected vapor, the front in the high flow rate test was observed to be faster than for the case of the low flow rate sample. The slower propagation in the experiment with a lower flow rate is perhaps due to the lower exerted pressure, allowing the condensed water to remain more easily in the porous matrix. In the higher flow rate experiment, the crack was observed to maintain less water compared to the lower flow rate case. In the later stages of the experiment, the water content in the matrix even exceeds the water content in the vicinity of the crack. The relative dryness of the crack compared to the porous matrix was first reported by Nemati et al. (2023) in the later stages of injection when the porous matrix became saturated with water. In this study, the smaller water content in the crack compared to the porous matrix was exacerbated at higher flow rates. This observation supports the reasoning that, along with capillary absorption, the exerted pressure, due to higher flow rates, further transferred the condensed water in the crack to further away or into the porous matrix. A higher flow rate of hot vapor can also increase the temperature in the fracture, reducing subsequent condensation and resulting in lower water content within the fracture. A sample with lower porosity was also tested at these same two flow rates. Due to the lower permeability of the porous matrix, saturation levels were roughly the same in the two cases as the vapor flow could not easily penetrate the matrix. Patches of water were also visible in the crack in both conditions; however, water accumulation was significantly less pronounced at the higher flow rate due to the vapor's exerted pressure. In the high flow rate case, these patches showed rapid transitions from one location to another (in a fraction of a second) and were only visible when studying individual radiographs. Such a transition resembles the avalanche event observed in infiltration processes in fractured porous media, as described by Wood et al. (2004) and Xue et al. (2023), involving the sudden release and rapid infiltration of a large volume of water.

The results indicate that a breakthrough is not observed in the sample without a fracture throughout the injection process (1700 s), while it occurs in 1100 s when a fracture is present. This is in line with Medjigbodo et al. (2016), where damaged concrete led to an increase in leakage rate under high temperature and pressure conditions (*i.e.*, 5 bar and 140 °Celsius). In these intense conditions, the evolution of crack openings plays a significant role due to coupled thermo-mechanical effects (Simon et al., 2007; Medjigbodo et al., 2013). Similar to the effect of the presence of a fracture, the increase in the flow rate by 36% and the decrease in matrix porosity by 3 times reduces the breakthrough time by approximately half. Comparing the condensed water observed inside the sample using neutron tomography to the net vapor content delivered to the sample through temperature boundary conditions can be a useful indicator of the amount of water that has leaked out of the sample. Decreasing matrix porosity by 0.05 (3 times decrease) was found to have the most profound effect, as a significant difference between the water content in the sample and the net delivered vapor to the sample was observed in low porosity samples (Fig. 3), suggesting that the condensed water leaks to the outside of the sample. Stable water content in the porous matrix below the water front is observed in all experiments, usually with a saturation in the range of 35%. However, in the low-flowrate, high-porosity experiment, lower injection pressure due to the fracture and higher porosity lead to saturation exceeding 50%. This suggests higher injection pressure enhances the gas's ability to sweep condensed water.

## 5. Conclusion

This study investigates water vapor condensation in fractured porous media, specifically sandstone, and explores the impact of the existence of a crack, matrix porosity, and the vapor flow rate. Cylindrical samples were collected from Fontainebleau sandstone and pre-fractured using a Brazilian splitting test in a feedback-controlled loop. A vapor and air mixture is injected at a constant flow rate, and rapid in situ neutron tomography, captured every 30 s, visualizes the time-resolved water migration. High neutron attenuation by hydrogen allows for tracking the condensed water in 3D and its migration within the porous matrix. The consistency between the overall water content measured by neutron tomography and the data from boundary measurements (temperature and flow rate) up until the breakthrough demonstrates the reliability of this method.

In summary, these tests show that:

- In the sample with a fracture, an initial water front appears in the fracture early on, indicating that the crack acts as a preferential path for vapor.
- The condensed water in the crack gets rapidly absorbed by the porous matrix due to capillary effects, preventing further water accumulation in the crack.
- The matrix's porosity significantly impacts this process, as lower porosity leads to quicker saturation and breakthrough.
- In the low porosity sample, the early saturation of the matrix leads to the accumulation of condensed water in the crack, forming evolving patches of water inside the fracture.
- Higher flow rates accelerate the propagation of the wetting front and result in less overall water remaining in the crack due to the comparatively high pressure pushing the water into the matrix.
- Breakthrough occurs faster in fractured samples and is further expedited by higher flow rates and lower matrix porosity.

The current experiments provide valuable insights into the mechanisms of water vapor condensation and transport in fractured sandstone. The corresponding 3D data has been made available to the research community. However, due to the experimental limitations of the setup and limited access to neutron facilities, it was not possible to test an even broader range of parameters. In future work, we will try to use this data to validate and calibrate a numerical model, allowing us to test more conditions and explore further the matrix of influencing parameters outlined above. This approach will make it possible to further distinguish the contributions of individual mechanisms at play, such as vapor condensation, capillary effect, and pressure-driven flow, and conduct a broader range of numerical experiments. By doing so, we can gain a deeper understanding of the complex interactions in fractured porous media and improve the predictability of water transport processes in such systems.

## CRediT authorship contribution statement

**Arash Nemati:** Writing – original draft, Visualization, Validation, Software, Methodology, Investigation, Formal analysis, Conceptualization. **Bratislav Lukić:** Writing – review & editing, Supervision, Methodology, Investigation, Funding acquisition, Data curation, Conceptualization. **Alessandro Tengattini:** Writing – review & editing, Resources, Methodology, Investigation. **Matthieu Briffaut:** Writing – review & editing, Supervision, Project administration, Funding acquisition, Conceptualization. **Philippe Séchet:** Writing – review & editing, Supervision, Resources, Project administration, Investigation, Funding acquisition.

## Declaration of competing interest

The authors declare the following financial interests/personal relationships which may be considered as potential competing interests: Bratsalv Lukic reports financial support was provided by Engineering and Physical Sciences Research Council. Arash Nemat reports financial support was provided by French National Research Agency. If there are other authors, they declare that they have no known competing financial interests or personal relationships that could have appeared to influence the work reported in this paper.

## Acknowledgments

This project is financed by the Labex Tec21 Investissements d'avenir - agreement n° ANR-11-LABX-0030 through a Ph.D. thesis. The authors acknowledge ILL for granting beamtime for proposal number 1-07-28 and 1-07–12. B.L. acknowledges funding from the EPSRC International Centre to Centre grant with ESRF (EP/W003333/1). This work is part of an in-house research programme at ID19 of ESRF for which beamtime within proposal IH-ES-64 is greatly acknowledged.

## Appendix

### *Brazilian test*

The fractures were initiated using the Brazilian test, where horizontal compression induces tensile stresses that split the sample along a vertical diameter, creating a single central crack while keeping the rest of the sample intact. A feedback-controlled splitting test (Fig. 15a) is used to generate aperture-controlled cracks where two LVDTs are fixed on opposite sides of the specimen to monitor the crack opening displacement (COD). Wooden layers are placed between the loading plates and the specimen to prevent damage at the loading points due to stress concentration. The test is controlled by a closed-loop feedback system that adjusts the loading ram based on the average displacement measured by the LVDTs. Due to the substantial height of the sample, the crack typically initiates at one end of the sample and propagates towards the opposite side. This results in a significantly greater displacement reading from one of the LVDTs. Once the targeted crack opening displacement of 200 μm is achieved and a visible crack is observed at both ends of the sample, the sample load is slowly released so as to ensure that the sample does not split into separate parts. Fig. 15b displays the relationship between crack opening displacement (COD) and tensile stress ($\sigma_t$) during the loading process. The tensile stress is defined as $\sigma_t = \frac{2P}{\pi LD}$, where $P$ is the applied load, $L$ is the sample length, and $D$ is the sample diameter.

### *Repeatibility*

The last experiment with low porosity and high flow rate (*Exp-05*) was repeated (*Exp-06*) on a comparable sample with similar characteristics and experimental conditions. Aside from modest local microstructural differences, a good degree of similarity is observed in the condensed water evolution in both cases, as shown in Fig. 16. Specifically, the qualitative behaviors discussed in Section 3.2 appear to be consistent. This agreement extends to the quantitative macroscopic measurements. For instance, the propagation of the wetting front of the condensed water is compared in Fig. 17. The standard deviation of the difference in the water front position is 1.2 mm, which is equivalent to 3% of the sample length.

## Data availability

Neutron data-sets are available at doi.org/10.5291/ILL-DATA.1-07-28 and doi.org/10.5291/ILL-DATA.1-07-12.

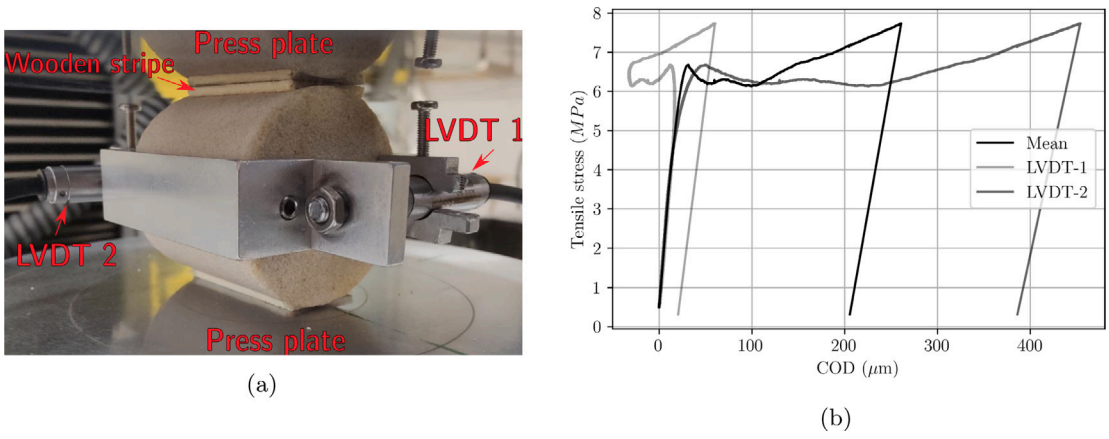


**Fig. 15.** (a) Brazilian test setup. (b) crack opening displacement (COD) versus tensile stress ($\sigma_t$) during the loading process.

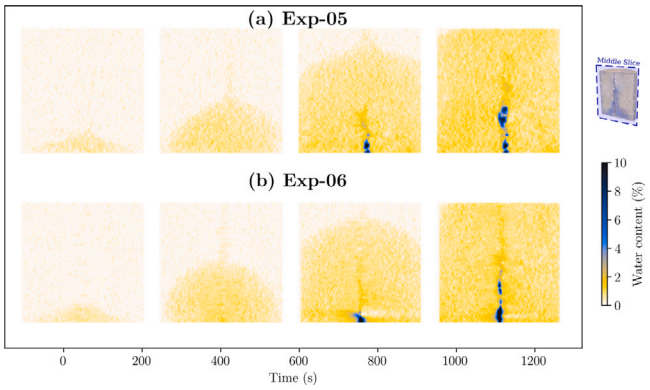


**Fig. 16.** Comparison of water content along the middle vertical slice at different stages of the injection process repeated on two comparable samples to test the repeatability (a) *Exp-05* and (b) *Exp-06*.

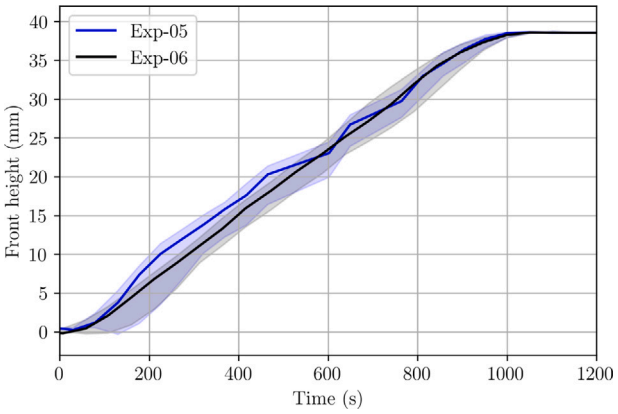


**Fig. 17.** The advancement of the water front in the porous matrix over time along the height repeated on two comparable samples to test the repeatability (a) *Exp-05* and (b) *Exp-06*.

## References


Bergins, C., Crone, S., Strauss, K., 2005. Multiphase flow in porous media with phase change. Part II: Analytical solutions and experimental verification for constant pressure steam injection. Transp. Porous Media 60 (3), 275–300. http://dx.doi.org/10.1007/s11242-004-5740-5.

Bertels, S.P., DiCarlo, D.A., Blunt, M.J., 2001. Measurement of aperture distribution, capillary pressure, relative permeability, and in situ saturation in a rock fracture using computed tomography scanning. Water Resour. Res. 37 (3), 649–662. http://dx.doi.org/10.1029/2000WR900316.

Boer, H., 1995. Mass flow controlled evaporation system. Le J. de Phys. IV 5 (C5), C5–961. http://dx.doi.org/10.1051/jphyscol:19955113.

Bourbie, T., Zinszner, B., 1985. Hydraulic and acoustic properties as a function of porosity in fontainebleau sandstone. J. Geophys. Res.: Solid Earth 90 (B13), 11524–11532. http://dx.doi.org/10.1029/JB090iB13p11524.

Brouwers, H.J., 1996a. An experimental study of constant-pressure steam injection and transient condensing flow in an air-saturated porous medium. J. Heat Transfer 118 (2), 449–454. http://dx.doi.org/10.1115/1.2825865.

Brouwers, H., 1996b. An experimental study of constant-pressure steam injection and transient condensing flow in an air-saturated porous medium. http://dx.doi.org/10.1115/1.2825865.

Bruining, J., Marchesin, D., 2006. Analysis of nitrogen and steam injection in a porous medium with water. Transp. Porous Media 62, 251–281. http://dx.doi.org/10.1007/s11242-005-1733-2.

Chaparro, M., Saaltink, M., 2016. Water, vapour and heat transport in concrete cells for storing radioactive waste. Adv. Water Resour. 94, 120–130. http://dx.doi.org/10.1016/j.advwatres.2016.05.004.

Chen, Y., Shi, M., Cheng, P., Peterson, G., 2008. Condensation in microchannels. Nanoscale Microscale Thermophys. Eng. 12, 117–143. http://dx.doi.org/10.1080/15567260701866702.

Chen, H., Wang, Z., Wang, K., Li, Z., Li, S., 2020. Investigation of EOR mechanism for flue gas assisted SAGD. J. Pet. Sci. Eng. 193, 107420. http://dx.doi.org/10.1016/j.petrol.2020.107420.

Class, H., Helmig, R., 2002. Numerical simulation of non-isothermal multiphase multicomponent processes in porous media.: 2. Applications for the injection of steam and air. Adv. Water Resour. 25 (5), 551–564. http://dx.doi.org/10.1016/S0309-1708(02)00014-3.

Class, H., Helmig, R., Bastian, P., 2002. Numerical simulation of non-isothermal multiphase multicomponent processes in porous media.: 1. An efficient solution technique. Adv. Water Resour. 25 (5), 533–550. http://dx.doi.org/10.1016/S0309-1708(02)00015-5.

Crone, S., Bergins, C., Strauss, K., 2002a. Multiphase flow in homogeneous porous media with phase change. Part I: Numerical modeling. Transp. Porous Media 49 (3), 291–312. http://dx.doi.org/10.1023/A:1016271213503.

Crone, S., Bergins, C., Strauss, K., 2002b. Multiphase flow in homogeneous porous media with phase change. Part I: Numerical modeling. Transp. Porous Media 49, 291–312. http://dx.doi.org/10.1023/A:1016271213503.

Dauti, D., Tengattini, A., Pont, S.D., Toropovs, N., Briffaut, M., Weber, B., 2020. Some observations on testing conditions of high-temperature experiments on concrete: An insight from neutron tomography. Transp. Porous Media 132 (2), 299–310. http://dx.doi.org/10.1007/s11242-020-01392-2.

El Kadi, K., Alnaimat, F., Sherif, S., 2021. Recent advances in condensation heat transfer in mini and micro channels: A comprehensive review. Appl. Therm. Eng. 197, 117412. http://dx.doi.org/10.1016/j.applthermaleng.2021.117412.

Fan, J., Cheng, X., Chen, Y.S., 2003. An experimental investigation of moisture absorption and condensation in fibrous insulations under low temperature. Exp. Therm Fluid Sci. 27 (6), 723–729. http://dx.doi.org/10.1016/S0894-1777(02)00305-9.

Fan, J., Cheng, X., Wen, X., Sun, W., 2004. An improved model of heat and moisture transfer with phase change and mobile condensates in fibrous insulation and comparison with experimental results. Int. J. Heat Mass Transfer 47 (10–11), 2343–2352. http://dx.doi.org/10.1016/j.ijheatmasstransfer.2003.10.033.

Forsyth, P.A., 1993. A positivity preserving method for simulation of steam injection for NAPL site remediation. Adv. Water Resour. 16 (6), 351–370. http://dx.doi.org/10.1016/0309-1708(93)90014-7.

Gupta, R., Lukić, B., Tengattini, A., Dufour, F., Briffaut, M., 2022. Experimental characterisation of transient condensed water vapour migration through cracked concrete as revealed by neutron and X-ray imaging: Effect of initial saturation. Cem. Concr. Res. 162, 106987. http://dx.doi.org/10.1016/j.cemconres.2022.106987.

Hu, J., Chao, C.Y., 2007. An experimental study of the fluid flow and heat transfer characteristics in micro-condensers with slug-bubbly flow. Int. J. Refrig. 30 (8), 1309–1318. http://dx.doi.org/10.1016/j.ijrefrig.2007.04.010.

Huang, H., Ye, C., Sun, W., 2008. Moisture transport in fibrous clothing assemblies. J. Engrg. Math. 61 (1), 35–54. http://dx.doi.org/10.1007/s10665-007-9201-3.

Hunt, J.R., Sitar, N., Udell, K.S., 1988. Nonaqueous phase liquid transport and cleanup: 2. Experimental studies. Water Resour. Res. 24 (8), 1259–1269. http://dx.doi.org/10.1029/WR024i008p01259.

Igwe, U., Khishvand, M., Piri, M., 2022. Retrograde condensation in natural porous media: An in situ experimental investigation. Phys. Fluids 34 (1), http://dx.doi.org/10.1063/5.0073801.

Kaestner, A.P., Trtik, P., Zarebanadkouki, M., Kazantsev, D., Snehota, M., Dobson, K.J., Lehmann, E.H., 2016. Recent developments in neutron imaging with applications for porous media research. Solid Earth 7 (5), 1281–1292. http://dx.doi.org/10.5194/se-7-1281-2016.

Karpyn, Z.T., Grader, A.S., Halleck, P.M., 2007. Visualization of fluid occupancy in a rough fracture using micro-tomography. J. Colloid Interface Sci. 307 (1), 181–187. http://dx.doi.org/10.1016/j.jcis.2006.10.082.

Kaslusky, S.F., Udell, K.S., 2002. A theoretical model of air and steam co-injection to prevent the downward migration of DNAPLs during steam-enhanced extraction. J. Contam. Hydrol. 55 (3–4), 213–232. http://dx.doi.org/10.1016/S0169-7722(01)00191-7.

Kim, S.-M., Kim, J., Mudawar, I., 2012. Flow condensation in parallel micro-channels–Part 1: Experimental results and assessment of pressure drop correlations. Int. J. Heat Mass Transfer 55 (4), 971–983. http://dx.doi.org/10.1016/j.ijheatmasstransfer.2011.10.013.

Lukić, B., Tengattini, A., Dufour, F., Briffaut, M., 2021. Visualising water vapour condensation in cracked concrete with dynamic neutron radiography. Mater. Lett. 283, http://dx.doi.org/10.1016/j.matlet.2020.128755.

Mcnamee, R.J., 2009. Fire Spalling – the Moisture Effect. In: 1st International Workshop on Concrete Spalling due to Fire Exposure, (No. September 2009).

Medjigbodo, S., Choinska, M., Regoin, J.P., Loukili, A., Khelidj, A., 2016. Experimental study of the air–steam mixture leakage rate through damaged and partially saturated concrete. Mater. Struct./Materiaux et Constr. 49 (3), 843–855. http://dx.doi.org/10.1617/s11527-015-0542-5.

Medjigbodo, S., Darquennes, A., Aubernon, C., Khelidj, A., Loukili, A., 2013. Effects of the air–steam mixture on the permeability of damaged concrete. Cem. Concr. Res. 54, 98–105. http://dx.doi.org/10.1016/j.cemconres.2013.08.013.

Nemati, A., Lukić, B., Tengattini, A., Briffaut, M., Séchet, P., 2024. Towards in-situ water quantification via neutron imaging: insights from NeXT-grenoble. Meas. Sci. Technol. 35 (7), 075405. http://dx.doi.org/10.1088/1361-6501/ad3cff.

Nemati, A., Lukić, B., Tengattini, A., Gupta, R., Briffaut, M., Séchet, P., 2023. Rapid in situ neutron tomography and X-ray imaging of vapor condensation in fractured sandstone. Transp. Porous Media 150 (2), 327–357. http://dx.doi.org/10.1007/s11242-023-02014-3.

Nield, D.A., Bejan, A., et al., 2006. Convection in porous media, vol. 3, Springer.

Ochs, S.O., 2006. Steam Injection into Saturated Porous Media – Process Analysis Including Experimental and Numerical Investigations – (Ph.D. thesis). Institut fur Wasserbau der Universitat Stuttgart.

Ogniewicz, Y., Tien, C., 1981. Analysis of condensation in porous insulation. Int. J. Heat Mass Transfer 24 (3), 421–429. http://dx.doi.org/10.1016/0017-9310(81)90049-1.

Qin, M., Aït-Mokhtar, A., Belarbi, R., 2010. Two-dimensional hygrothermal transfer in porous building materials. Appl. Therm. Eng. 30 (16), 2555–2562. http://dx.doi.org/10.1016/j.applthermaleng.2010.07.006.

Rabone, J., Carre, H., La Borderie, C., 2023. Steam flows in concrete cracks: Thermal behaviour. Nucl. Eng. Des. 413, 112551. http://dx.doi.org/10.1016/j.nucengdes.2023.112551.

Rüdiger, F., Dentz, M., Nimmo, J., Kordilla, J., 2022. Laboratory experiments and dual-domain modeling of infiltration dynamics in partially saturated fractured porous media. Vadose Zone J. 21 (2), e20177. http://dx.doi.org/10.1002/vzj2.20177.

Simon, H., Nahas, G., Coulon, N., 2007. Air-steam leakage through cracks in concrete walls. Nucl. Eng. Des. 237 (15-17 SPEC. ISS.), 1786–1794. http://dx.doi.org/10.1016/j.nucengdes.2007.03.025.

Sözen, M., Vafai, K., 1990. Analysis of the non-thermal equilibrium condensing flow of a gas through a packed bed. Int. J. Heat Mass Transfer 33 (6), 1247–1261. http://dx.doi.org/10.1016/0017-9310(90)90255-S.

Tengattini, A., Lenoir, N., Andò, E., Giroud, B., Atkins, D., Beaucour, J., Viggiani, G., 2020. NeXT-Grenoble, the neutron and X-ray tomograph in Grenoble. Nucl. Instrum. Methods Phys. Res. A 968, 163939. http://dx.doi.org/10.1016/j.nima.2020.163939.

Tengattini, A., Lenoir, N., Andò, E., Viggiani, G., 2021. Neutron imaging for geomechanics: A review. Geomech. Energy Environ. 27, 100206. http://dx.doi.org/10.1016/j.gete.2020.100206.

Tötzke, C., Kardjilov, N., Lenoir, N., Manke, I., Oswald, S.E., Tengattini, A., 2019. What comes NeXT? – High-speed neutron tomography at ILL. Opt. Express 27 (20), 28640. http://dx.doi.org/10.1364/OE.27.028640.

Tremsin, A., Shinohara, T., Oikawa, K., Li, J., Monteiro, P., 2019. Non-destructive mapping of water distribution through white-beam and energy-resolved neutron imaging. Nucl. Instrum. Methods Phys. Res. A 927 (February), 174–183. http://dx.doi.org/10.1016/j.nima.2019.02.037.

Udell, K.S., 1985. Heat transfer in porous media considering phase change and capillarity—the heat pipe effect. Int. J. Heat Mass Transfer 28 (2), 485–495.

van Aarle, W., Palenstijn, W.J., Cant, J., Janssens, E., Bleichrodt, F., Dabravolski, A., De Beenhouwer, J., Joost Batenburg, K., Sijbers, J., 2016. Fast and flexible X-ray tomography using the ASTRA toolbox. Opt. Express 24 (22), 25129. http://dx.doi.org/10.1364/OE.24.025129.

Wang, Y., de Hoop, S., Voskov, D., Bruhn, D., Bertotti, G., 2021. Modeling of multiphase mass and heat transfer in fractured high-enthalpy geothermal systems with advanced discrete fracture methodology. Adv. Water Resour. 154, 103985. http://dx.doi.org/10.1016/j.advwatres.2021.103985.

Wood, T., Glass, R., McJunkin, T., Podgorney, R., Laviolette, R., Noah, K., Stoner, D., Starr, R., Baker, K., 2004. Unsaturated flow through a small fracture–matrix network: Part 1. Experimental observations. Vadose Zone J. 3 (1), 90–100. http://dx.doi.org/10.2136/vzj2004.9000.

Wu, H., Cheng, P., 2005. Condensation flow patterns in silicon microchannels. Int. J. Heat Mass Transfer 48 (11), 2186–2197. http://dx.doi.org/10.1016/j.ijheatmasstransfer.2004.12.034.

Xue, S., Yang, Z., Zhou, Z., Hu, R., Chen, Y.-F., 2023. Influence of liquid splitting behavior at intersections on infiltration dynamics in an unsaturated fracture network. Water Resour. Res. 59 (10), e2023WR034639. http://dx.doi.org/10.1029/2023WR034639.

Zhang, Y., Peng, X., Conte, I., 2007. Heat and mass transfer with condensation in non-saturated porous media. Numer. Heat Transfer, Part A: Appl. 52 (12), 1081–1100. http://dx.doi.org/10.1080/10407780701453800.